Crystal plasticity analysis of cylindrical indentation on a Ni-base single crystal superalloy

Prajwal A. Sabnis [a], Samuel Forest [a], Nagaraj K. Arakere [b,*], Vladislav A. Yastrebov [a]

[a] MINES ParisTech, Centre Des Matériaux, CNRS UMR 7633, BP 87, 91003 Evry Cedex, France
[b] Mechanical and Aerospace Engineering, 237 MAE-B Building, University of Florida, Gainesville, FL 32611-6300, USA

A B S T R A C T

Crystal plasticity simulations and experiments of cylindrical indentation on Nickel base single crystal superalloy specimens are presented and discussed. The subsurface stress and strain fields presented are similar to those observed in meso-scale dovetail joints in single crystal turbine blades. Load is applied in the [001] primary orientation while the secondary orientation of the single substrate is varied. The secondary orientations [$\bar{1}$10] and [010] are examined at room temperature. The plastic zone below the indent is analysed in terms of the activated slip systems. The Finite Element predictions are compared to the detailed experimental observation of slip lines on the free lateral surface of the substrate. Results presented are of particular relevance to the understanding of slip localisation in single crystal dovetail contacts and subsequent crystallographic crack nucleation and propagation induced by subsurface shear stresses.

© 2013 Elsevier Ltd. All rights reserved.

1. Introduction

Nickel Base Single Crystal (NBSX) superalloy turbine blades used in high performance aircraft and rocket engines, are subject to high operating temperatures and high monotonic and cyclic stresses in a highly corrosive environment. Aircraft turbine mission profiles are often characterised by multiple throttle excursions, which shifts attention to fatigue and fracture considerations associated with areas below the blade platform which contain various stress risers in the form of buttresses and attachments. These stress concentration features are prone to contact fatigue damage, and can result in crystallographic initiation and crack growth along octahedral planes (Deluca and Annis, 1995; Arakere and Swanson, 2002). A quantitative description of the fatigue crack nucleation process in a single crystal anisotropic contact is far from complete. Some factors that are considered to play an important role in fatigue crack nucleation are the magnitudes of resolved shear stress on the slip planes and the normal stress on the slip plane with the highest resolved shear stress (Nalla et al., 2002). To better identify crack nucleation mechanisms, an understanding of evolution and localisation of plastic slip in single crystal meso-scale contacts, where the stress state is strongly triaxial, is essential. The anisotropic elastic and plastic properties of single crystal specimens depend on crystal orientation. In metallic single crystals, crack nucleation in regions of stress concentration is typically preceded by cyclic slip localisation. The growth of nucleated cracks is also preceded by plasticity at the crack tip. Thus, both initiation and propagation of cracks are influenced by elastic and plastic anisotropic material properties, and consequently by crystallographic orientation. Fracture toughness of single crystals has also been found to be dependent on both primary and secondary orientation of single crystals (Shrivastava and Ebrahimi, 1997; Gumbsch et al., 1998; Ebrahimi and Kalwani, 1999; Arakere and Swanson, 2001; Arakere and Swanson, 2002; Ranjan and Arakere, 2008).

---

* Corresponding author.
  E-mail address: nagaraj@ufl.edu (N.K. Arakere).

Examples of fretting/contact damage is often observed in the regions where the blade-root is attached into the turbine-disk. The material deterioration usually begins with either crystallographic or non-crystallographic damage initiation, and is often followed by crack propagation along crystallographic planes. Thus, an understanding of the fracture process in NBSX alloys is essential in evaluating the fatigue life of turbine-blades. To foster such an understanding, the study of localised plastic deformation (which usually precedes damage initiation) in NBSX superalloys is a necessary step. While there exist many experimental studies addressing the evolution of macro-level-plasticity in this kind of materials, to the authors' knowledge, there are few studies that are aimed at an analysis of sub-surface behaviour. Many instances of material-damage-initiation and micro-crack-propagation are observed to occur in the sub-surface layers of the material. Consequently, the following article presents a tool to aid in the necessary analysis of localised sub-surface fields in NBSX specimens.

A study of literature related to indentation on NBSX superalloys reveals a few interesting applications of indentation experiments. Indentation experiments have been used extensively to measure hardness and mechanical behaviour of materials. Indentation provides a convenient means for investigation and better understanding of the elastic limit and incipient plasticity in crystals. In recent years there has been considerable interest in the study of micro- and nano-scale indentation of anisotropic bulk materials, layered and functionally graded materials, and single crystals, to understand scale-dependent mechanical behaviour. Xu et al. (2009) use experimental indentation to study creep properties of an NBSX material, and use the Crystal Plasticity Finite Element Method (CPFEM) to investigate the effect of varying the primary orientation of the crystal, on the creep surface-morphology (see Xu et al., 2008) in an NBSX material. Eidel (2011) presents an experimental study and a CPFEM investigation of a pyramidal indentation on a CMSX-4 specimen. Brinell-type indentation of CMSX-4 single crystal substrate is considered by Zambaldi et al. (2007) to relate the plastic strain field induced on the indented surface at room temperature and recrystallisation phenomena occurring at higher temperatures. Comparisons between experimental and finite element results are provided regarding the anisotropy of sink-in or pile-up formation on the deformed surface. Arakere et al. (2006) present 2D and 3D numerical techniques to investigate subsurface stresses anisotropic materials, and apply these techniques to simulate cylindrical indentation on a NBSX material. Results from a simulated contact model are also presented as an interesting alternative to using a numerically-intensive conventional finite-element-method -based contact algorithm. Other recent articles on dislocation nucleation and plasticity during indentation of single crystals have been published by Tymiak et al. (2001), Zhu et al. (2004), Deshpande et al. (2004), Balint et al. (2006), Nicola et al. (2007), Kysar et al. (2007) and Casals and Forest (2009).

The mentioned contributions mainly address the deformation of the indented surface, especially the formation of pile-up or sink-in. The configuration studied in the present paper is very different since slip is observed on the lateral surface and not the indented surface so that insight is gained on the plasticity below the indentor, which is possible thanks to the choice of a cylindrical indentation instead of usual Berkovich or Brinell indentation. The case of cylindrical indentation handled in the present contribution corresponds to significantly different mechanical loading conditions and is especially relevant for the behaviour of blade footings. Experimental results of this type in single crystal superalloys are very scarce and their interpretation by means of crystal plasticity finite element simulations is unique. The simulations will explain the experimentally observed strong dependence of the plastic zone size and shape below the indentor depending on the secondary orientation, the primary orientation being kept to [001]. That is why the presented work contains original contributions in this important field of crystal plasticity of Nickel-based superalloys. Accordingly, the paper provides a complementing perspective to indentation compared to existing literature, and which is better suited to the turbine blade footing.

As already stated, the following article aims to address the analysis of sub-surface fields. To this end, numerical simulations were conducted using standard crystal plasticity material models. The details of the material model used in the simulations are discussed in the following sections. The results are then post-processed to generate dominant-slip-maps (as discussed in Sabnis et al., 2012), which are then used to analyse the deformation fields in the NBSX substrate.

Dovetail joints are used to secure compressor and turbine blades to disks in turbine engines. The rotational loads (body forces) of the jet engine turbine blades are reacted at the dovetail joints. The contact locations, their area of contact and contact stress are a complex function of geometry and clearance between the parts. The resulting contact stresses can be quite high, leading to localised yielding. Fretting results from blade vibration, which perturbs both the normal and tangential loads at the contact, resulting in contact fatigue loading. Gas turbine mission profiles are often characterized by multiple throttle excursions associated with maneuvers such as climb, intercept and air-to-air combat. This type of loading shifts attention to fatigue and fracture considerations associated with areas below the blade platform, which contain various stress risers in the form of attachments (Arakere and Swanson, 2001). The gas turbine industry is moving toward a design philosophy that stresses damage tolerance and threshold based designs, which has prompted the study of micromechanics of single crystal contacts, localised plasticity, crack initiation and other events that affect HCF life. Hence the study evolution of plasticity in cylindrical single crystal meso-scale contacts is very much pertinent.

A study of sub-surface plasticity/slip field development in cylindrical single crystal contact that is relevant to meso-scale blade attachment type of contacts is presented in the following sections. A cylindrical indentation experiment on a substrate closely represents the geometry of the section that is in contact with the disk. From a theoretical perspective, two alternative configurations could be considered for the proposed study. The first configuration would use a NBSX cylindrical indent on a hardened-steel substrate. While this configuration represents more closely the setup of a blade attachment, practical considerations concerning the production of an NBSX indent lead to experimentation using the second configuration. The second configuration consists of NBSX substrates upon which indentation tests are conducted. In the study presented here, a hard-
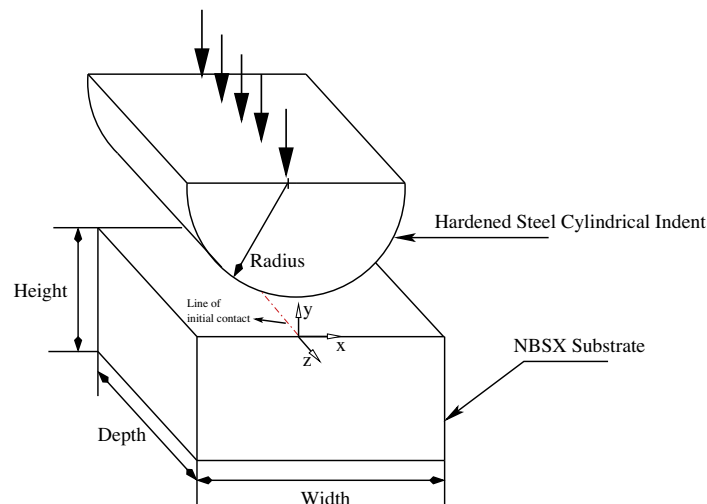
Fig. 1. Schematic representation of the indentation set-up.

ened steel roller bearing was used as an indent. A schematic representation of the numerical experiment used in the study is shown in Fig. 1.

Due to the highly anisotropic nature of this class of materials, the indentation experiments and simulations were carried out for two secondary orientations of the substrate. The two crystal orientations considered for the substrate materials are defined with respect to the substrate frame *XYZ*, *Y* being the normal direction to the indentation plane. *Z* is the direction normal to the observation plane, see Fig. 1. The two orientations are the following:

- Orientation A: $[\bar{1}10]\|X$, $[001]\|Y$, $[110]\|Z$
- Orientation B: $[010]\|X$, $[001]\|Y$, $[100]\|Z$

The present work is structured as follows. Section 2 provides a detailed description of the experimental procedures carried out in the study. It is followed by a description of the numerical aspects of the simulations (Section 3). The results of the analysis are presented in Section 4 in terms of slip system activity. They are then discussed in relation to experimental observations of slip lines on the free lateral surface of the substrate. In particular, CPFEM is used to show the significant differences between slip activation on the free surface and in the bulk, which may have implications for the behaviour of turbine blades. Results presented have both engineering and scientific relevance to the analysis and fatigue design of single crystal superalloy turbine blades.

Regarding notations used throughout this work, first, second and fourth rank tensors are denoted by $\underline{\mathbf{a}}$, $\underset{\sim}{\mathbf{A}}$ and $\underset{\approx}{\mathbf{A}}$, respectively.

2. Material and experimental procedures

PW1480 single crystals of Ni-base superalloy castings in the form of two 25 mm diameter (1 inch) bars with cylinder axis along the [001] direction were provided in as-heat-treated condition by Pratt and Whitney. The microstructure of the alloys consisted of cubical primary γ' precipitates in a matrix of solid solution γ. Both crystals did not have any noticeable eutectic pools or pores. Laue X-ray back-reflection technique was employed to identify the crystallographic orientations of them, based on which the samples' directions were realised. Although this material consists of two phases (Face Centred Cubic (FCC) γ-matrix and L1$_2\gamma'$-precipitate), in the case where particle shearing takes place at room temperature, geometrically, plastic deformation is analogous to a FCC single crystal. The γ' phase is an intermetallic. Consequently, these materials have a Critical Resolved Shear Stress (CRSS) that is an order of magnitude higher than pure Al or Cu. The advantage of using a superalloy crystal is that it yields at considerably high applied stresses and therefore the applied load levels at small plastic zones can be accurately controlled and measured. It should be pointed out that the [001] primary orientation direction in turbine blade castings is also controlled to within 8–10°.

The yield stress for the considered single crystal superalloy was evaluated by conducting tensile tests along the [001] direction using dog-bone samples with rectangular cross-sections. The analysis of deformation bands on the face and the sides of samples revealed that slip took place along the {111} planes (Ebrahimi et al., 2006; Westbrooke, 2005; Ebrahimi and Westbrooke, 2008). Assuming the activation of octahedral slip systems, the average CRSS value was measured to be 324 MPa.

Fig. 2 shows the slip traces observed on the free surfaces for the two orientations used in the cylindrical indentation experiments. The theoretically expected slip traces are shown in Fig. 5. For Orientation A, slip traces extending up to a depth
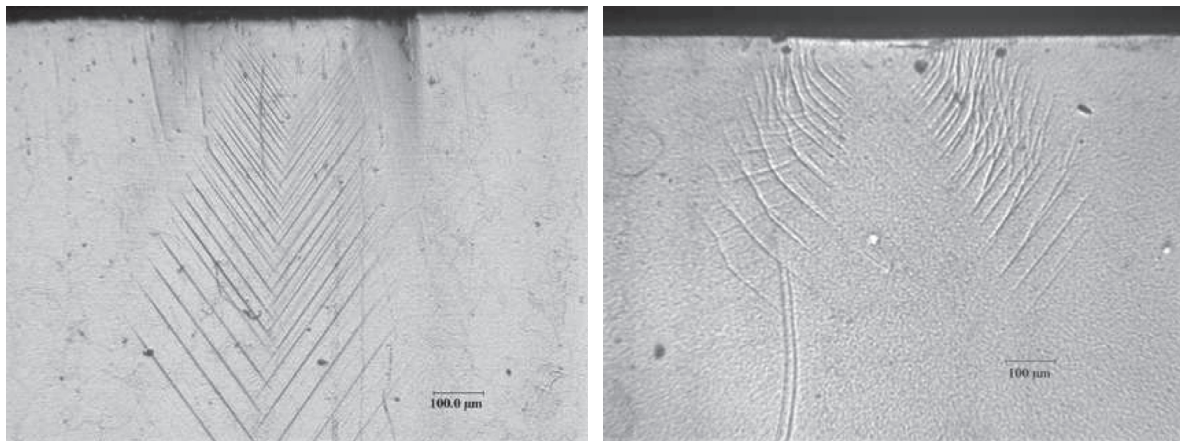
(a) Orientation A at 500 μm contact

(b) Orientation B at 325 μm contact

Fig. 2. Experimental slip traces observed.

of approximately 800 µm are observed on the free surface. The most prominent slip bands are found in a 550 µm wide region, directly below the line of initial contact (see Fig. 1). For Orientation B, the slip lines extend up to a depth of 300 µm. The slip traces observed on the free surface of Orientation B are spread over a width of approximately 760 µm at a contact length of 325 µm.

3. Computational analysis

In the present study, the elasto-plastic deformation of the NBSX substrate is addressed by a combination of cubic elasticity and crystal plasticity material models. The cylindrical indent is treated as an isotropically elastic solid. The actions/reactions of contact forces on the indent/substrate are simulated by a suitable contact algorithm. These behaviours are incorporated in the nonlinear finite element framework Zset (see Besson and Foerch, 1997).

3.1. Finite element mesh

Two types of meshes are considered in this work. *Mesh 1* represents the full geometry shown in Fig. 1. It can be used for non-symmetric orientations of the single crystal. In particular, it will be used to test the effect of small deviation from ideal crystal orientations. However, the geometry of the system and the main orientations of the single crystal substrate considered in this work allow for reduction of the mesh size due to symmetry reasons. For the two orientations considered in this work, one quarter of the previous mesh is sufficient to predict the full stress–strain field. This second finite element mesh is called *Mesh 2*.

Mesh 1 is constructed by the extrusion in the Z-direction of a 2D quadratic-element mesh. The extrusion of the 2D mesh contains 10 elements along the thickness, with a higher element density near the free surface of the specimen. The concentration of elements is focused towards the free surface since high strain gradients are expected in the region due to the fulfilment of the traction free surface conditions. The contact line between the indent and the substrate (corresponding to a contact length of 500 µm on the top edge of the free surface), was meshed with 40 quadratic elements of equal length with reduced integration. The finite elements of *Mesh 1* are 20-node quadratic bricks and 15-node prismatic elements, with reduced integration.

Mesh 2 represents one quarter of the NBSX substrate used in experiments, thus requiring symmetry boundary conditions in both X- and Z- directions. It consists of linear elements with reduced integration because, in conjunction with the contact algorithm, it was found to be computationally faster. Mesh 2 is slightly coarser than mesh 1 with regards to the free surface (31 nodes over a length of 125 µm in mesh 2, as compared to 41 nodes over a length of 125 µm in mesh 1). This difference in densities is due to the choice of quadratic elements in *Mesh 1* as compared to linear elements in *Mesh 2*. It is noted that, for the indentation loads considered in this study, there were no remarkable differences in the fields observed by either of the two meshes. The finite elements of *Mesh 2* are 8-node linear bricks and 6-node prismatic elements, with reduced integration.

A greater number of layers along the thickness with the concentration focused towards the free surface is understandably preferable, as it allows for a better estimation of the gradients near the free surface. However, increasing the number of elements in the thickness also increases the computational effort required for the resolution of the problem by significant amounts. Computational characteristics such as number of degrees of freedom (DOFs), numbers of elements and computational memory required for the resolution of the non-linear problem for some of the meshes used in the simulations are given in Table 2. Results from various simulations are presented in the following sections. The results presented contain 10 and 20 elements along the thickness of the specimen (for *Mesh 1* and *Mesh 2* respectively), unless otherwise specified. Both the

generated meshes, *Mesh 1* and *Mesh 2*, are shown in Figs. 3 and 4 respectively. The dimensions used for the experimental and numerical specimens are indicated in Table 1.

3.2. Crystal plasticity and material parameters

For the numerical modelling of crystal plasticity, Mandel (1973) suggested a generalised formulation in which a multiplicative decomposition of the deformation gradient tensor $\mathbf{F}$, into elastic and plastic parts $\mathbf{F}_e$ and $\mathbf{F}_p$ is postulated. The plastic part $\mathbf{F}_p$ maps the inelastic deformations onto a intermediate configuration, in which there is no rotation of the material microstructure with respect to the reference orientation. The rotations/lattice distortions are then introduced via the elastic part of the split $\mathbf{F}_e$.

$$\mathbf{F} = \mathbf{F}_e \mathbf{F}_p \tag{1}$$

Based on this multiplicative split of the deformation gradient tensor, the Green–Lagrange strain tensor can be introduced as

$$\mathbf{E} = \frac{1}{2}\left[\mathbf{F}_e^T \mathbf{F}_e - \mathbf{1}\right] \tag{2}$$

Introducing the Piola Kirchhoff stress tensor $\mathbf{\Pi}$ as

$$\mathbf{\Pi} = J_e \mathbf{F}_e^{-1} \boldsymbol{\sigma} \mathbf{F}_e^{-T} \tag{3}$$

and the Mandel stress tensor $\mathbf{M}$ as

$$\mathbf{M} = J_e \mathbf{F}_e^T \boldsymbol{\sigma} \mathbf{F}_e^{-T} \tag{4}$$

the stress power can be rewritten as

$$J \boldsymbol{\sigma} : \dot{\mathbf{F}} \mathbf{F}^{-1} = \mathbf{\Pi} : \dot{\mathbf{E}} + \mathbf{M} : \dot{\mathbf{F}}_p \mathbf{F}_p^{-1} \tag{5}$$

In is noted that the $J = \det(\mathbf{F})$, $J_e = det(\mathbf{F}_e)$. In metals, plastic deformation is isochoric, thus $J_p = \det(\mathbf{F}_p) = 1$.

The introduction of the stress power into the generalised local dissipation relation yields the elasticity state law as

$$\mathbf{\Pi} := \rho \frac{\partial \psi}{\partial \mathbf{E}} = \mathbf{C} : \mathbf{E} \tag{6}$$

where $\mathbf{C}$ is a fourth order tensor representing the elastic moduli. The above relation is obtained upon the assumption of a quadratic potential w.r.t. $\mathbf{E}$. As mentioned earlier, the anisotropic nature of NBSX crystals is captured by the use of cubic crystal elasticity. Due to reasons of crystal symmetry, $\mathbf{C}$ can be represented as a 6×6 matrix characterised by three material parameters.
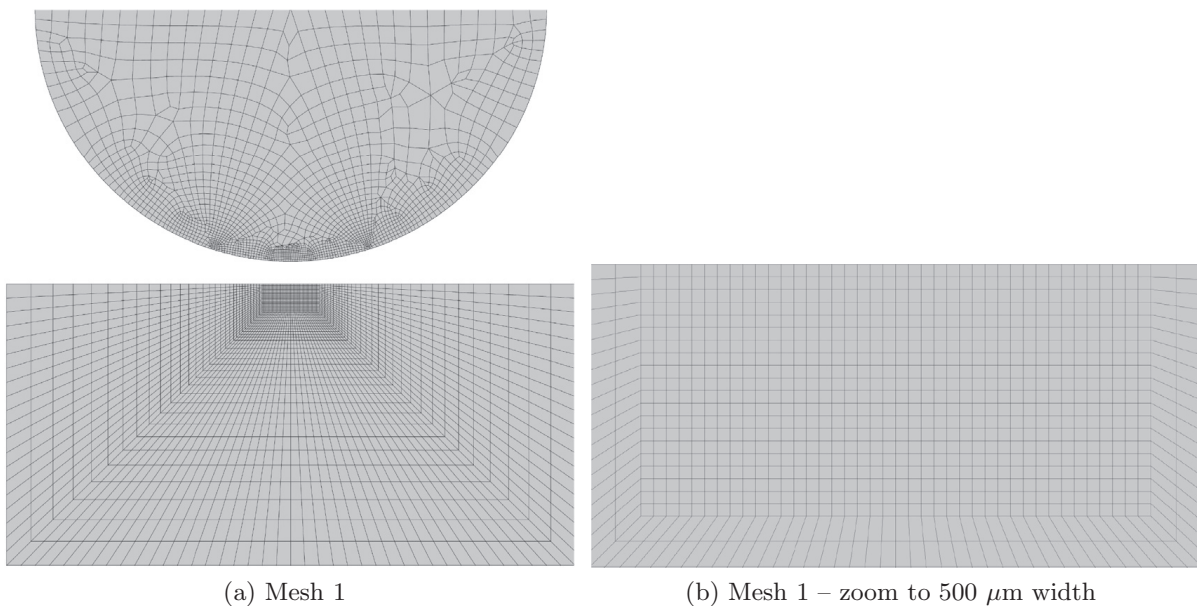

(a) Mesh 1   (b) Mesh 1 – zoom to 500 μm width

Fig. 3. Mesh 1 used corresponding to the full indentation setup.

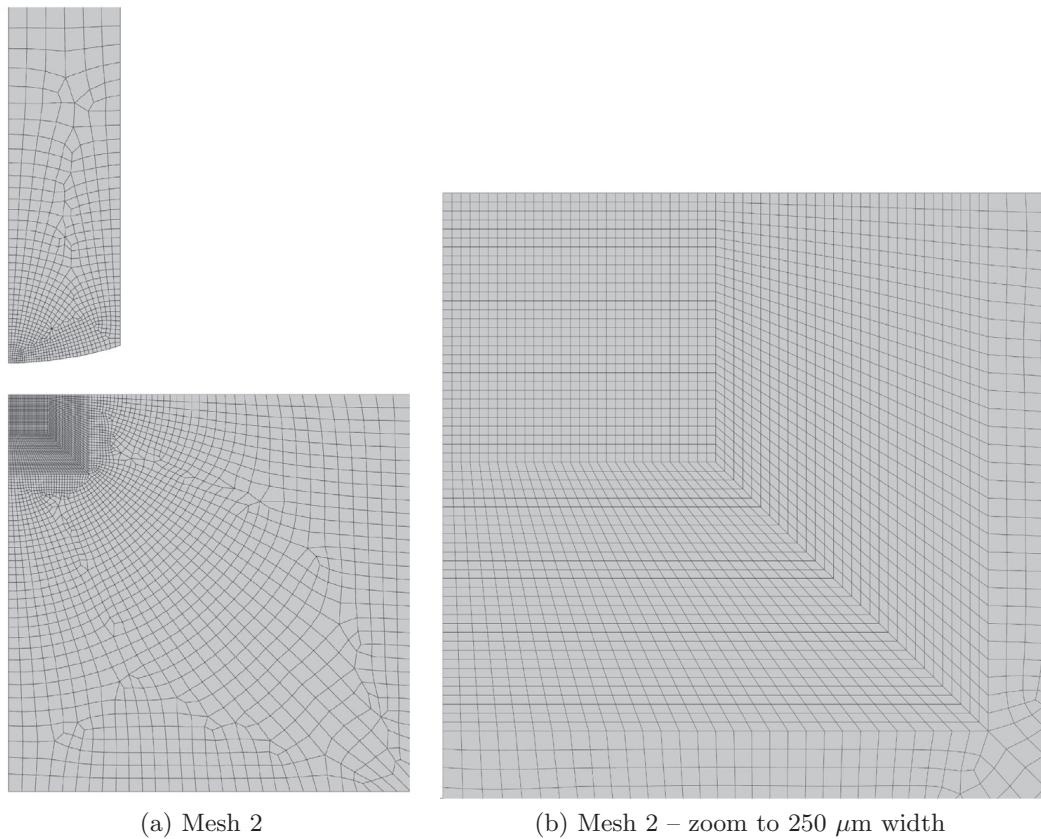(a) Mesh 2   (b) Mesh 2 – zoom to 250 μm width

Fig. 4. Mesh 2 corresponding to one quarter of the indentation setup.

Table 1
Dimensions of the specimens tested.

Specimen dimensions (in mm)	
Width	5.0
Depth	8.5
Height	2.5
Radius of indent	2.25

Table 2
Computational details for symmetric quarter specimen.

	Number of elements along thickness		
	10 Elements	16 Elements	20 Elements
Mesh 1			
Total number of elements in mesh	50,210	–	–
Number of elements in NBSX substrate	40,003	–	–
Number of elements in Hardened Steel indent	18,207	–	–
Number of DOFs	665,499	–	–
Memory required (Mb)	17,083	–	–
Mesh 2			
Total number of elements in mesh	53,420	85,472	106,840
Number of elements in NBSX substrate	45,780	73,248	91,560
Number of elements in Hardened Steel indent	7640	12,224	15,280
Number of DOFs	182,688	282,336	348,768
Memory required (Mb)	2167	4504	6859

The evolution of the plastic slip is modelled as a multimechanism problem with an internal variable γ^s being assigned to each slip system *s*. The evolution of γ^s is controlled by the implementation of the Schmid criterion, according to which plas-

ticity commences only after the resolved shear stress τ^s reaches a certain critical resolved shear stress, τ^c. The resolved shear stress which is given as

$$\tau^s = \underset{\sim}{\mathbf{M}} : (\underline{\mathbf{l}}^s \otimes \underline{\mathbf{m}}^s) \tag{7}$$

is introduced into the yield criterion, which is given by

$$f_p^s = |\tau^s| - \tau_c \tag{8}$$

$\underline{\mathbf{l}}^s$ and $\underline{\mathbf{m}}^s$ are the slip direction and the normal to the slip plane respectively. The evolution of γ^s is controlled by a classical Norton type power law. In Eq. (9), large values of n and low values of K lead to an almost ideal elastic–plastic behaviour in the usual range of strain rates.

$$\dot{\gamma}^{s} = \left\langle \frac{|\tau^s| - \tau_c}{K} \right\rangle^n \operatorname{sign}(\tau^s) \tag{9}$$

The evolution of the plastic part of the deformation gradient $\underset{\sim}{\mathbf{F}}_p$ is given by the relation

$$\underset{\sim}{\dot{\mathbf{F}}}_p \underset{\sim}{\mathbf{F}}_p^{-1} = \sum_{s=1}^{12} \dot{\gamma}^s (\underline{\mathbf{l}}^s \otimes \underline{\mathbf{m}}^s) \tag{10}$$

In the simulations presented here, linear isotropic hardening is included

$$\tau_c = R_0 + H \nu^s, \tag{11}$$

with

$$\dot{\nu}^s = |\dot{\gamma}^s|, \tag{12}$$

where R_0 is the initial critical resolved shear stress and H is the hardening modulus. No interaction between slip systems was introduced in the hardening rule (11). The fact that the interaction matrix in constitutive models that do not consider the two-phase nature of nickel base superalloys, is the identity matrix is not an oversimplification but the result of identification from complex multiaxial tests on single crystals, as summarised in the reference (Nouailhas et al., 1995) where the Schmid law was tested under various loading conditions. This is a specific feature of nickel-based superalloys, strongly different from usual aluminum or copper alloys, that is probably due to the microstructure made of periodic distributions of cuboidal coherent precipitates. This does not mean that there is no interaction between dislocations inside the channels of the γ phase but it tells us that the identification of a macroscopic effective model based on Schmid law for nickel-based superalloys leads to an identity matrix. The extra-hardening induced by possible latent hardening coefficients was not observed in the multislip multiaxial configurations experimentally studied in the 1990s especially at low temperature, even at moderate plastic strain levels.

It is worth noting that in small strain formulations with linearised strain tensors, the Mandel stress $\mathbf{M}$ in Eq. (7) can be replaced by the Cauchy stress $\boldsymbol{\sigma}$ as the two become equivalent. Furthermore, in small-strain formulations, the multiplicative split of the deformation gradient tensor leads to an additive split of the total infinitesimal strain tensor ($\boldsymbol{\varepsilon}$) into elastic and plastic parts ($\boldsymbol{\varepsilon}^e$ and $\boldsymbol{\varepsilon}^p$ respectively). This split is given as

$$\underset{\sim}{\boldsymbol{\varepsilon}} = \underset{\sim}{\boldsymbol{\varepsilon}}^e + \underset{\sim}{\boldsymbol{\varepsilon}}^p \tag{13}$$

For the infinitesimal case, the plastic strain rate is derived from Eq. (10) as

$$\underset{\sim}{\dot{\boldsymbol{\varepsilon}}}^p = \sum_{s=1}^{12} \dot{\gamma}^s \left(\frac{1}{2} (\underline{\mathbf{l}}^s \otimes \underline{\mathbf{m}}^s + \underline{\mathbf{m}}^s \otimes \underline{\mathbf{l}}^s) \right) \tag{14}$$

The choice of the viscoplatic Norton law (9) ensures the uniqueness of system selection for a given stress tensor. The chosen values for the material parameters are $n = 15$ and $K = 4$ MPa s$^{1/n}$). They are such that the response does not display any noticeable strain rate sensitivity in the range of strain rates covered by the simulations. The critical resolved shear stress is $\tau_c = 324$ MPa identified from tensile tests on various orientations according to Sabnis et al. (2012). The slight hardening modulus is $H = 75$ MPa.

Alternative hardening and flow rules can be found in the classical references Asaro (1983) and Pierce et al. (1983).

3.3. Determination of slip system activity

A typical NBSX superalloy consists of an FCC lattice structure, which indicates the presence of 12 octahedral slip systems on 4 slip planes. In addition to these principal slip systems, Nickel-base superalloys also exhibit macroscopic plastic slip along 6 cubic slip systems (see Méric et al., 1991). Macroscopic cube slip lines have been observed in the past in tensile specimens loaded in the direction $\langle 1\,1\,1 \rangle$, see Méric et al. (1991). However, cube slip lines are not observed on the lateral surface of the samples studied in the present work. They were not observed at the free surface of the notched specimens considered by Sabnis et al. (2012) either. Also it could not be proved that macroscopic cube slip takes place at a crak tip in single crystal

superalloys by Flouriot et al. (2003), although some traces were ambiguous (two possibilities {1 1 1} or {0 0 1} plane trace). No physical explanation is currently available for that but this is a rather common observation on non-homogeneously deformed single crystal superalloys. This macroscopic analysis of slip lines is to be distinguished from the types of dislocations in TEM observations in γ channels. As a result of the experimental macroscopic observations, cube slip was not introduced in the simulations. The simulations presented in this paper incorporate only octahedral slip (i.e. slip along the 12 octahedral slip systems). The definitions of the slip systems used in the simulations are shown in Table 3.

Since the slip-systems' definitions and the crystal orientations of the tested specimens are known, it is possible to determine the expected slip traces on the observable free surface of the specimen (plane normal to Z direction). These are shown in Fig. 5. The slip traces correspond to the intersection of the slip plane of the considered slip system with the observation surface plane. The angles of the traces obtained by such an analysis, with respect to the loading axis, can then be used to identify the slip traces that are found experimentally on the free surface. In the case of symmetric crystal orientations however, the same trace can correspond to two possible slip planes, see for example Fig. 5. These experimental observations can be combined with finite element computations in order to determine the most probable activated slip plane.

Three distinct slip systems can contribute to deformation along one slip plane. All of them do not necessary lead to a visible slip trace on the observation plane. For instance if the slip direction $\underline{l}^s$ of system s is parallel to the observation plane, then the motion of dislocation will not induce any step on the free surface. To make this distinction, a *Visibility index* (VI) is introduced (Sabnis et al., 2012). The VI is defined as the scalar product of the slip direction and the normal to the observed free surface. The VI is computed for each individual octahedral slip system in Table 3. A VI = 0.0 indicates that the slip system is not expected to produce a visible trace on the free surface. Correspondingly, a greater VI indicates that prominent slip traces are expected. This differentiation provides a tool for a better comparison between simulated results and experimental observations.

3.4. Dominant slip system maps

The obtained CPFEM results provide stress, strain fields, slip activity and lattice rotation of the substrate under deformation. However, the application of post-processing methods to these results may provide further insights into various mechanisms that are active in the material. One such post-processing technique was introduced in an earlier publication (Sabnis

Table 3
Definition of slip systems used in the crystal plasticity model and the visibility index of each slip system for the different orientations tested.

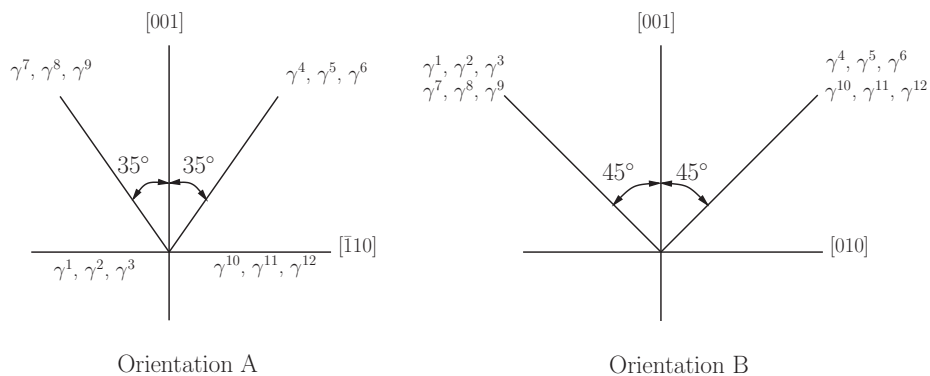| Slip system number	Normal to slip plane $\underline{m}^s$	Slip direction $\underline{l}^s$	Visibility index	
			Orientation A	Orientation B
1	(1 1 1)	[$\bar{1}$ 0 1]	0.5	0.707
2	(1 1 1)	[0 $\bar{1}$ 1]	0.5	0.0
3	(1 1 1)	[$\bar{1}$ 1 0]	0.0	0.707
4	(1 $\bar{1}$ 1)	[$\bar{1}$ 0 1]	0.5	0.707
5	(1 $\bar{1}$ 1)	[0 1 1]	0.5	0.0
6	(1 $\bar{1}$ 1)	[1 1 0]	1.0	0.707
7	($\bar{1}$ 1 1)	[0 $\bar{1}$ 1]	0.5	0.0
8	($\bar{1}$ 1 1)	[1 1 0]	1.0	0.707
9	($\bar{1}$ 1 1)	[1 0 1]	0.5	0.707
10	(1 1 $\bar{1}$)	[$\bar{1}$ 1 0]	0.0	0.707
11	(1 1 $\bar{1}$)	[1 0 1]	0.5	0.707
12	(1 1 $\bar{1}$)	[0 1 1]	0.5	0.0

Fig. 5. Theoretical slip traces observed on the free surface normal to Z axis for both considered orientations.

et al., 2012). The method analyses the plastic slips (γ^s) on each individual slip-system, in order to determine the slip system(s) with the maximum amount of slip (absolute value) at each stored time step, at each Gauss point. Then, each point is assigned an index corresponding to the label of the slip system with the *Dominant plastic slip*. The resulting maps are the dominant slip system maps, referred to henceforth as *γ-maps*.

The γ-maps represent only the most active slip system and should not be confused with an indication on the number of simultaneously activated slip systems at a given points. The generation of γ-maps requires a threshold to differentiate between active and inactive slip systems, this threshold is chosen to be an amount of slip equal to 10^{-7} in our simulations. Such zones with plastic deformation below this minimum level are assigned an index of 0, which indicates purely elastic domains.

The post-processing applied chooses the slip system with maximum slip by serial comparison of slip systems in an ascending order. If for example, one considers only the octahedral slip systems, then the procedure compares the plastic slip by pairs, beginning at slip systems 1 and 2, and then proceeding to system 2 and 3 or 1 and 3 (based on the outcome of the comparison between 1 and 2). This feature is particularly useful in the case of multiple slip systems having the same maximum amount of plastic slip. In such a case, the index corresponding to the slip system occurring at the latest in the comparison queue is assigned as the index of the Gauss point. Furthermore, a negative sign is placed ahead of the index to indicate that other slip systems are exhibiting same amounts of slip activity.

3.5. Numerical algorithms

In this section we give a brief description of numerical algorithms employed in this work, that are implemented in the finite element suite Z-set, see Besson and Foerch (1997). For integration of the constitutive equations for the crystal plasticity model we used a specific implementation of the theta-method according to Chaboche and Cailletaud (1996) coupled with an adaptive time-stepping algorithm. The global non-linear problem, which is formulated within the finite element method, is solved by the classical Newton–Raphson method. To introduce contact constraints (non-penetration/non-adhesion), we used the direct flexibility method by Zienkiewicz et al. (1995) and Jean (1995). In this approach the contact constraints are fullfilled on abstract node-to-face contact elements, see Wriggers (2006), each of them contains one node (slave) from one contacting surface and one face from another surface (master). In contrast to widely used penalty and Lagrange multipliers techniques, this direct approach leads to a better global convergence, because nonlinearities associated with the material's behaviour and the contact are treated separately.

4. Results

A direct comparison is drawn between the computational prediction of slip activity at the free surface and the experimentally observed slip lines for two single crystal orientations.

### 4.1. Comparison of computed γ-maps with experimental observations

Cylindrical indentation was simulated for substrate single crystal orientations A and B up to a contact length of 500 μm in the plane normal to Z. The γ-maps were determined at several loading steps. The comparison of FE results with experimental ones is carried out by superimposing the dominant slip maps onto the optical micrographs of the experimental specimens. An analysis of the γ-maps shows that the plastic slip zones predicted by CPFEM have dimensions close to the experimental values. This can clearly been seen in Fig. 6. The slip systems predicted by CPFEM are compared in a more systematic way with the slip lines in the optical microscope images, while considering the VIs presented in Table 3, the angles of the expected slip lines (Fig. 5) and the magnitude of the individual slip systems predicted by the CPFEM.
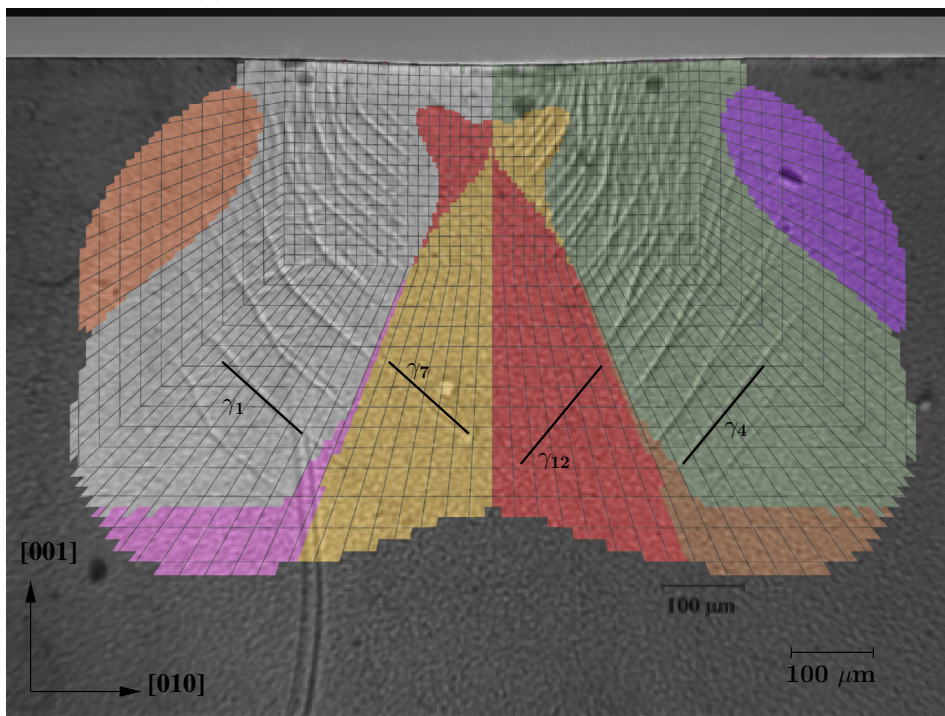
4.1.1. Orientation A

For Orientation A, slip traces are experimentally observed up to a distance of 800 µm below the indent for an indentation depth $\delta = 19$ µm. The width of the region containing slip lines reaches 550 µm for a contact length of 500 µm. The dominant slip systems in the lateral lobes for Orientation A have a zero visibility index according to Table 3 (slip system 10), This indicates that there is no contradiction between experiment and computation. The depth of the simulated plastic zone in the observation plane is slightly underestimated as compared to the experimentally observed depth of slip lines.

The dominant slip system map shown in Fig. 6(b) shows an analysis of the post-processed results, which have been superimposed onto the optical micrograph image. The solid black lines show the trace for the dominant slip system identified in the post-processed maps. The zones where the most-active slip systems are identified as systems 4, 5, 7, 9 and 10, are in good agreement with the slip traces observed in experiments. The zones where slip systems 11 and 12 are predicted to be the most active do not correspond to the inclined slip traces observed on the surface of the experimental specimen. The experimental slip traces rather hint at the dominance of slip systems 4 and 7 in these regions.

Focusing on the region where system 12 was identified as the dominant slip system, a comparison of Fig. 2(b) with the expected slip lines in Fig. 5 indicates the systems 7–9 as the most probable candidates for the position of the "most-active-slip-system" in the region. Upon examination of the plastic slip on each individual system in the CPFEM, systems 8 and 9 are ruled out as they present no activity in the region under consideration. Furthermore, the values of slip on the systems 7 and
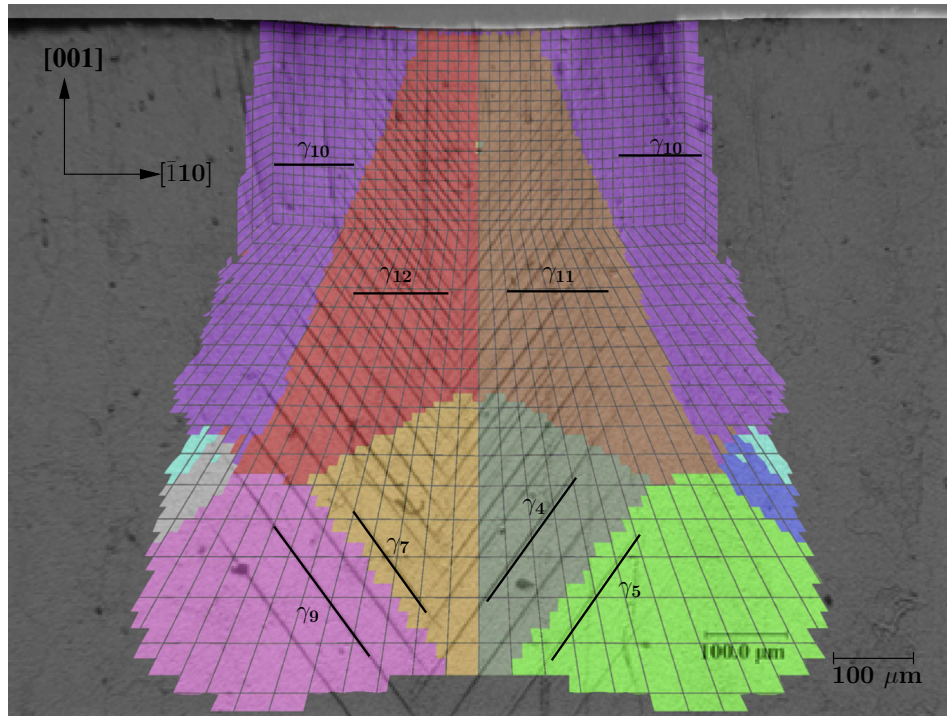
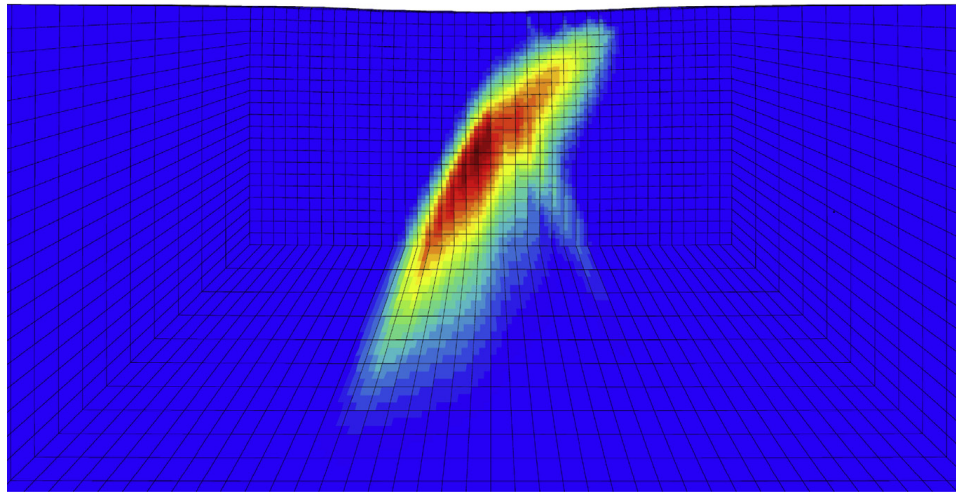(a) Orientation A at 500 μm contact with indent

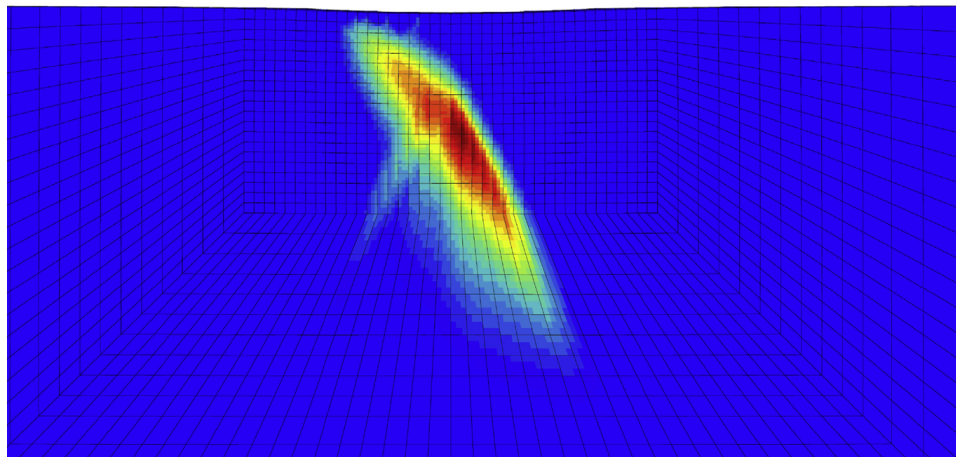(b) Orientation B at 325 μm contact with indent

(c) Scale indicating the different slip systems represented in the γ–maps

Fig. 6. Comparison of dominant slip maps (γ-maps) and experimental results for an indentation depth $\delta = 19$ μm for (a) and $\delta = 30$ μm for (b).

12 are found to be very close (≈ 0.027) over a major part of the region in question. Keeping in mind the fact that the systems 7 and 12 have the same VI, we conclude that these slip systems exhibit similar levels of activity. It is interesting to note that

(a) Plastic slip on slip system 7

(b) Plastic slip on slip system 12

| 1e-07 | 0.0037 | 0.007 | 0.011 | 0.014 | 0.018 | 0.022 | 0.026 | 0.029 | 0.033 | 0.037 | 0.041 | 0.045 |
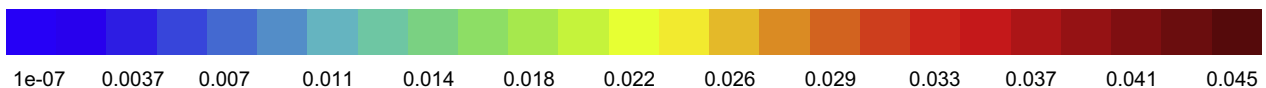
Fig. 7. Iso-values of plastic slip for systems 7 and 12 (orientation B).

the combined application of γ-maps and VI allows for a more focused analysis of slip systems. In the present case, two slip systems (7 & 12) out of the 12 available systems are identified as the most probable dominant systems.

Another feature that is observed in Fig. 6(b), is that the axis of symmetry between the slip lines (which is expected to be in-line with the loading axis) is at an angle of about 8° to the vertical axis. This deviation from the expected slip traces could be due to a misorientation of the primary [0 0 1] direction. A confirmation of the angle of deviation from the ideal orientation by experimental techniques such as Laue measurement is necessary, such a confirmation of misorientation may shed light on some sort of a bias towards system 7 over system 12 in the experiment. In the absence of such analysis, further simulations of the experiment which account for some misorientation in the material, are suggested. Such simulations were conducted and are discussed in a later section (see Section 5.3).

4.1.2. Orientation B

In Orientation B, slip traces are seen in a region that extends up to 540 μm below the indent and about 760 μm wide at a contact length of 325 μm. For Orientation B where two small lateral lobes are observed according to the simulation in Fig. 2(b) in the absence of observed slip traces.

Two major lateral plastic zones that are observed in the γ-maps for Orientation B match the slip traces observed on the experimental specimens. The γ-maps also indicated two central domains dominated by the slip systems 7 and 12 in the γ-maps, whereas no slip lines are observed in the experiment in these zones. A closer inspection of the VI values for Orientation B indicates that the slip systems 7 and 12 are not expected to produce any visible slip traces (i.e. VI = 0) for this surface orientation. Thus, the presence of plasticity on these systems cannot be confirmed by optical examination alone.
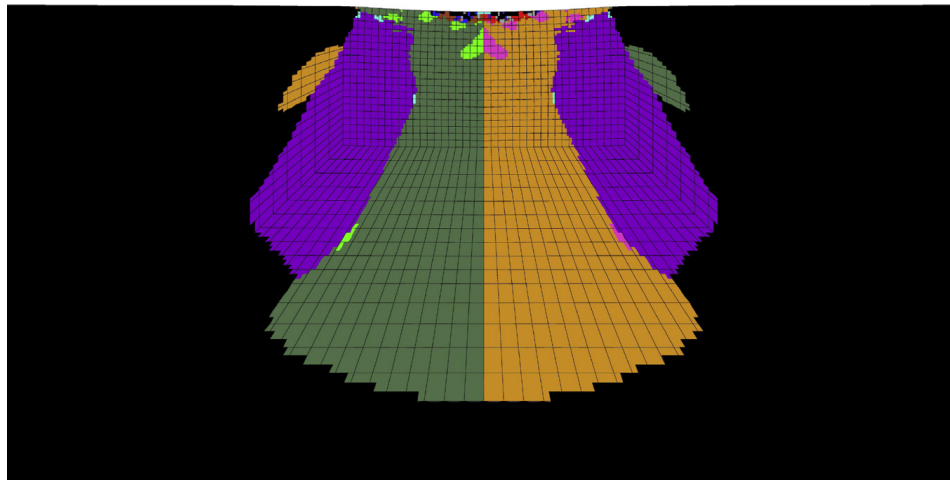
(a) Orientation A at 500 μm contact length
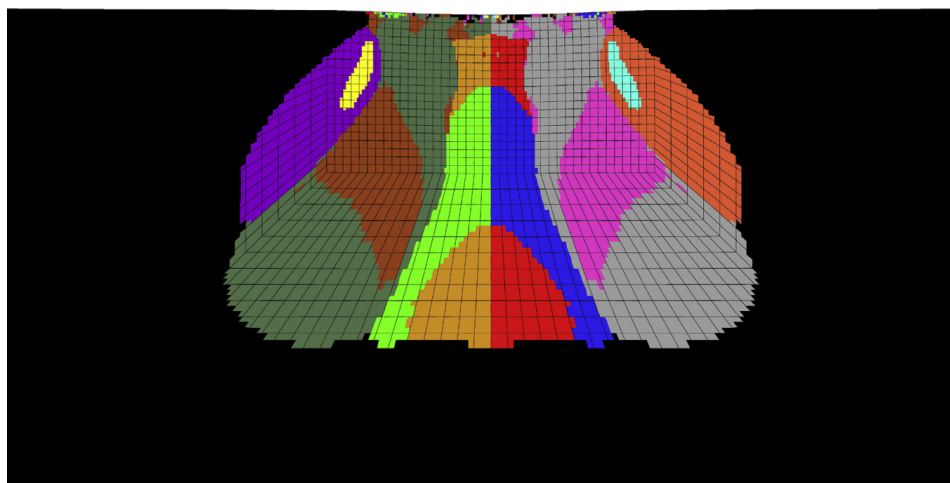
(b) Orientation B at 325 μm contact length

Fig. 8. Slip activity at the core of NBSX substrates. To be compared with the γ-maps in Fig. 6.

It is also noted that some intense curved bands occur in the experimental images. These intense bands are symmetric about the [0 0 1]-axis and overlap with other slip lines on the surface. To confirm the existence of such more intense deformation zones, the individual amount of plastic slip on each slip plane was examined. The CPFEM simulations indicate a significant strain localisation due to the slip systems 7 and 12, which seems to correspond to the localisation bands observed in the specimen. The computed contours of plastic slip on these two systems are shown in Fig. 7. However, the simulated results need to be confirmed with further testing such as strain field measurements by microgrid or digital image correlation.

5. Discussion

The FE simulations presented in the previous section provide additional information that could shed light on the differences between slip activity at the free surface and in the bulk of the specimen. These aspects are addressed in the following section. Lattice rotation fields and crystal misorientation effects close the discussion.

5.1. Surface vs. bulk behaviour

The CPFEM reveals a rapid variation of plastic strain along the thickness of the simulated specimen. The plastic strain field observed at the free surface changes drastically at a distance of $\approx$ 320 µm from the free surface (see Fig. 10). The bulk plastic field then stabilises and becomes invariant along the Z-axis. The γ-maps in the core for both the specimens are shown in Fig. 8. Comparing these γ-maps with the γ-maps in Fig. 6, obvious differences in shape and size of the plastic zone and nature

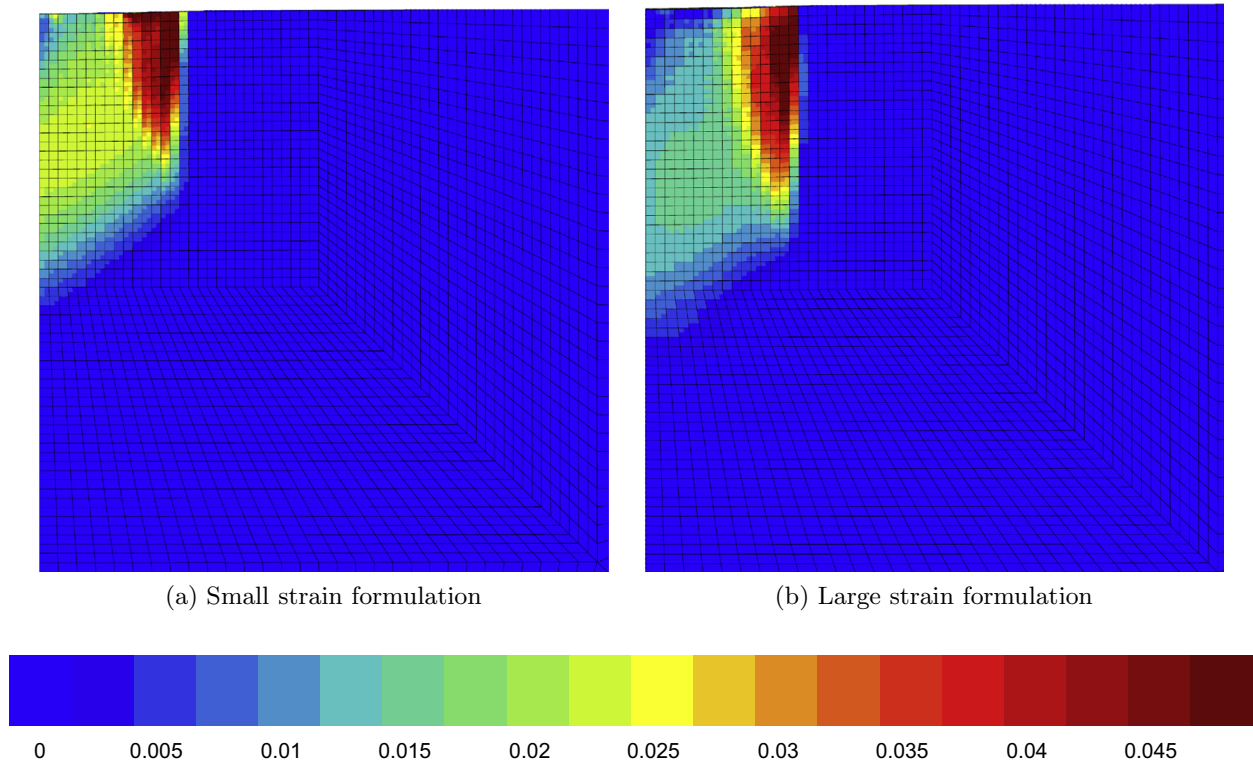(a) Small strain formulation   (b) Large strain formulation

Fig. 9. Equivalent plastic strain field for FE computations using the small strain formulation of the model (b) and the finite deformation model (a), for Orientation A at a contact length of 140 μm.
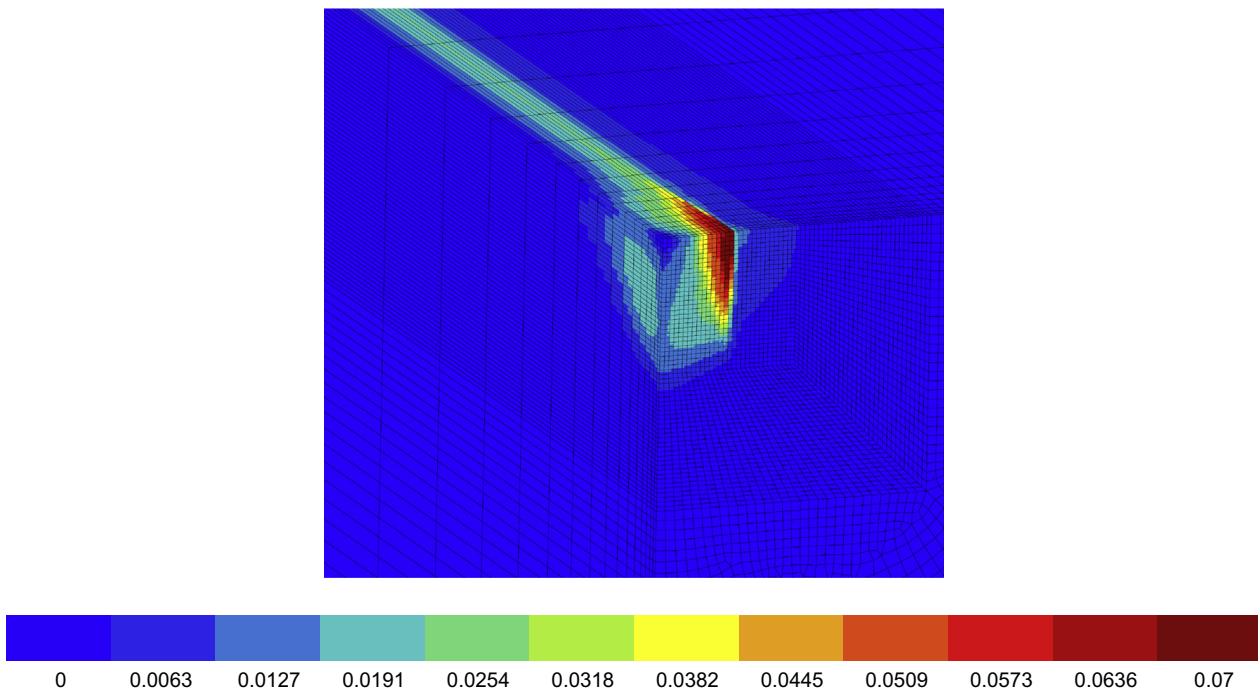

Fig. 10. Variation of lattice rotation in Orientation A specimen at a contact length of 140 μm (in radians).

of dominant slip systems, are observed between the core and the free surface. These differences are the consequences of plane stress conditions at the free surface and to symmetry conditions in the core. This indicates that the analysis of such experiments should not be based solely on the observation of the free surface and that complementary destructive analyses are required inside the sample. Such different bulk and free surface behaviours were already noted in the simulation of
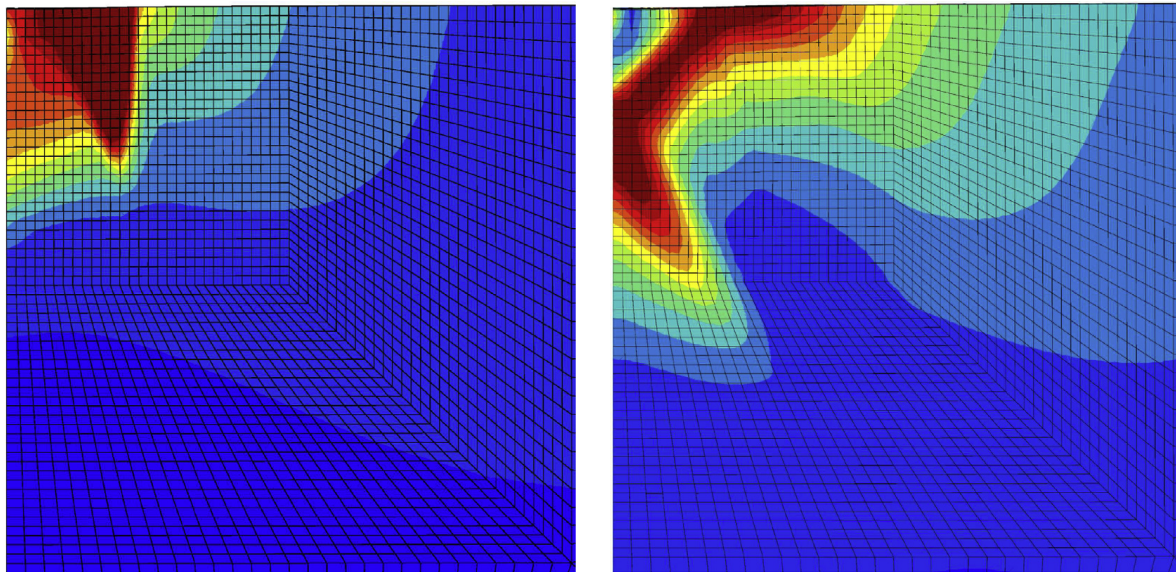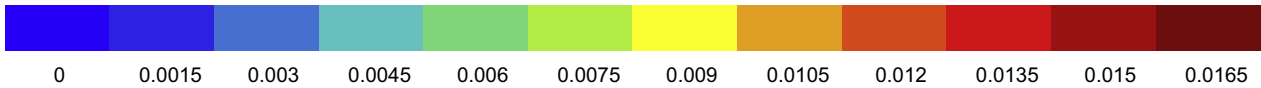
(a) Orientation A   (b) Orientation B

Fig. 11. Comparison between the lattice rotations in the two secondary orientations at a contact length of 140 μm (in radians).
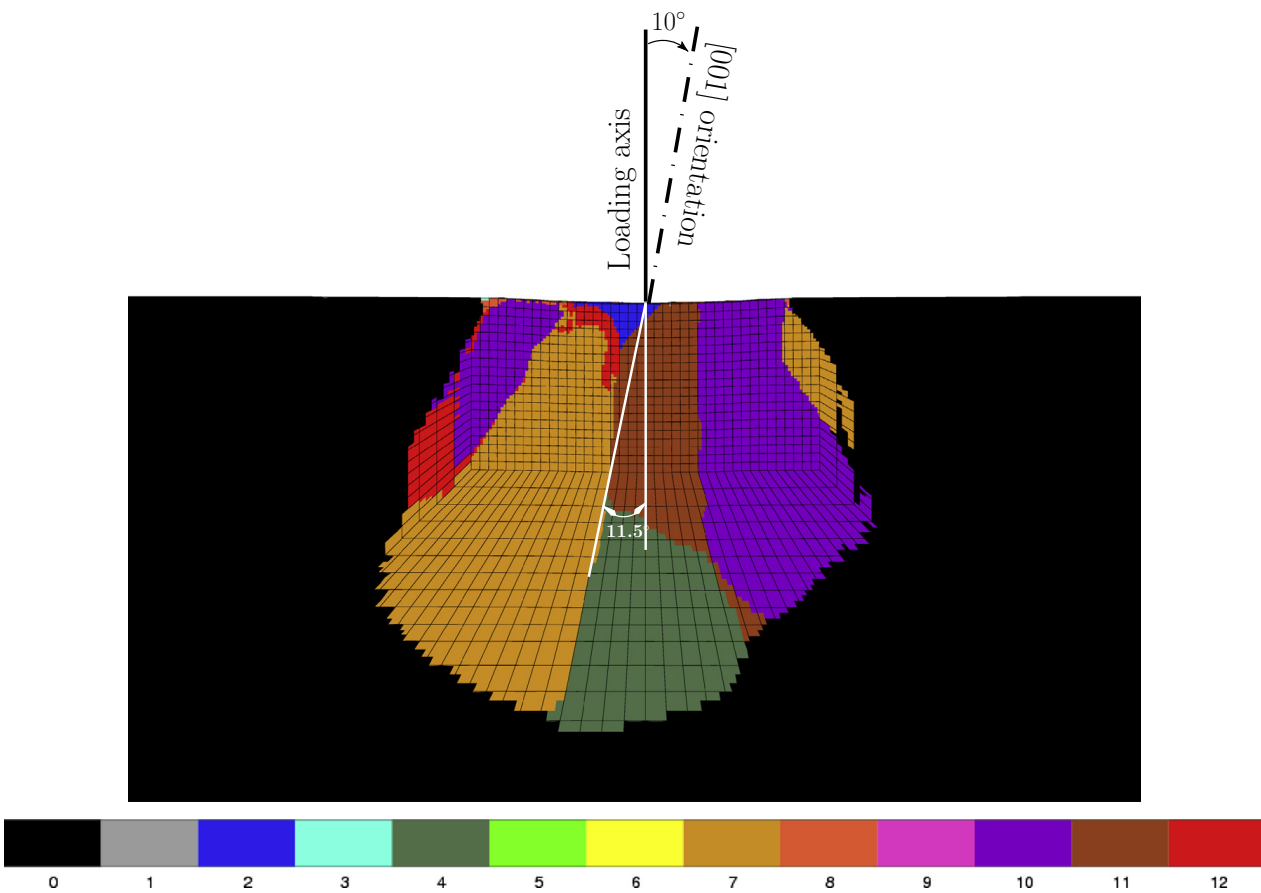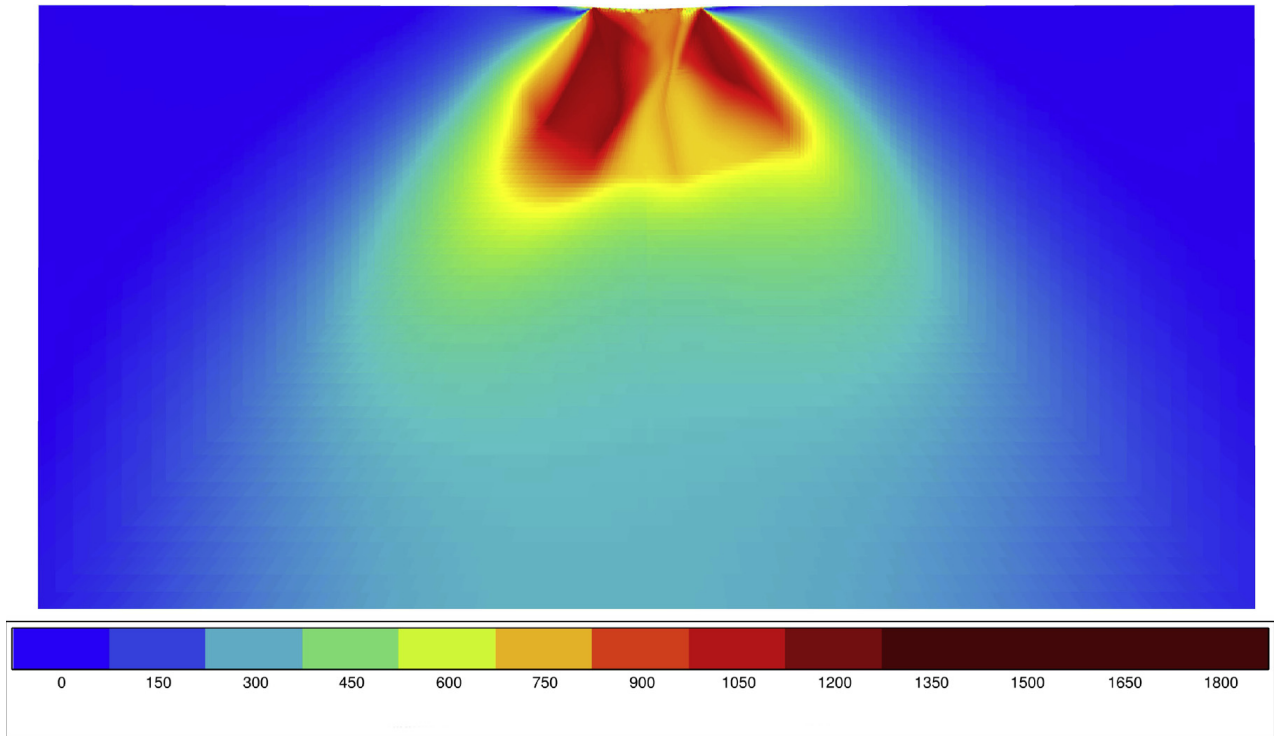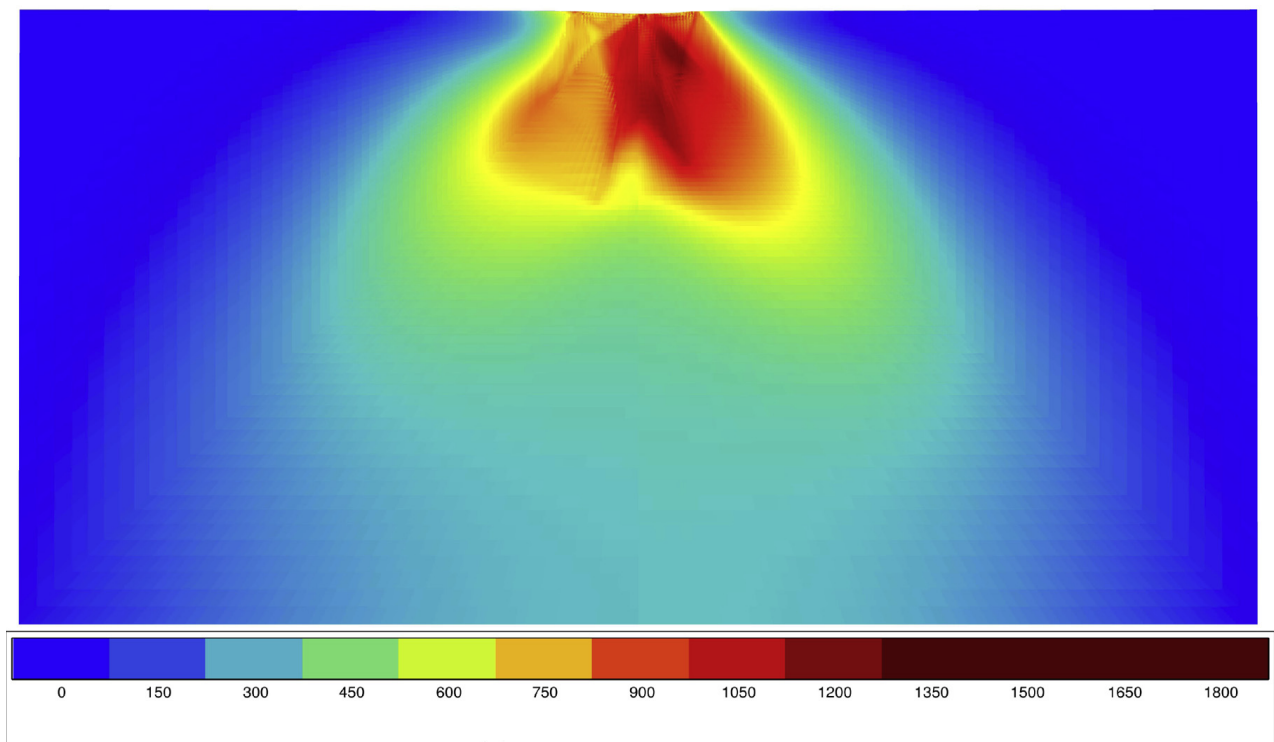

Fig. 12. Dominant slip map in specimen with Orientation A. A misorientation of 10° was introduced in the simulation.

(a) Specimen core

(b) Specimen free surface

Fig. 13. Von Mises stress in Orientation A specimen. 10° misorientation was introduced for the simulation.

cracks in single crystal superalloy CT specimens, see Flouriot et al. (2003). In the reference Kysar and Briant (2002), the specimens were cut at the middle section and an EBSD (Electron Back-Scattering Diffraction) analysis was performed, thus revealing parts of the bulk material response. The surface effect was also pointed out in the case of flat double notched specimens in Sabnis et al. (2012).
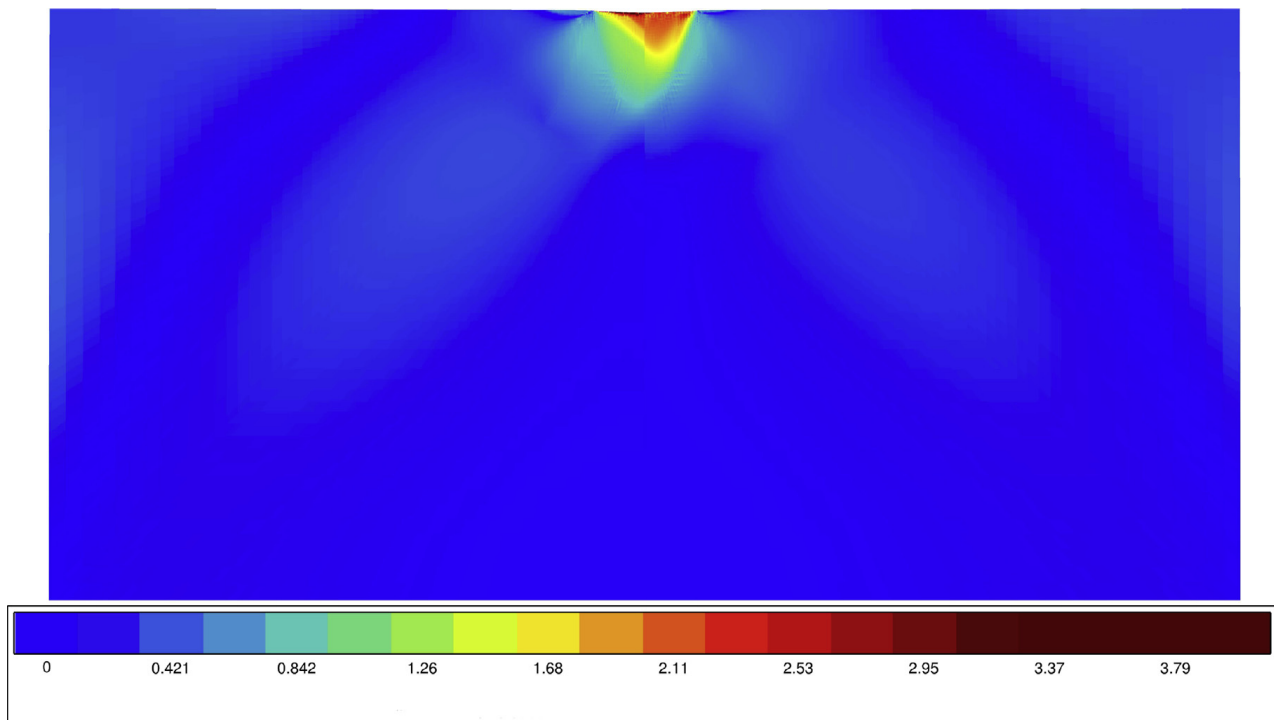
Fig. 14. Stress triaxiality at the core in the Orientation A specimen. 10° misorientation was introduced in the simulation.

5.2. Small- vs. finite-strain formulation

The results of Finite Element simulations obtained by means of the finite strain and of the small strain versions of the crystal plasticity model (see Section 3.2) were compared for loading conditions encountered in the experiments. The small strain version of the model is computationally less expensive in terms of CPU time, which is an advantage for practical structural computations involving single crystals like in turbine blades. Fig. 9 shows a comparison between the equivalent plastic strain field predicted by the small- and large-strain formulations, in Orientation A at a contact length of 140 μm. Differences can be observed but remain insignificant especially with respect to the purpose of comparison with experimental results.

The finite deformation formulation of the model also provides information about lattice rotations in the single crystal material. The Figs. 10 and 11 show the lattice rotations for orientations A and B. At a contact length of 140 μm, Orientation A shows a maximum rotation of 0.077 radians (i.e. about 4.5°) and Orientation B shows a maximum rotation of 0.02 radians (about 1°). From Fig. 11, one can observe that the lattice rotation patterns are very different for the two orientations. This indicates that the secondary orientation also affects, in a profound manner, the lattice rotation development in the specimen.

It is noted that the results discussed in Sections 5.1 and 5.2 are presented at a contact length of 140 μm, whereas the other results are discussed at larger contact lengths. This choice was made so as to enable a comparison between the *finite strain*- and *infinitesimal strain*-formulations of the crystal plasticity model. The simulations using the finite deformation formulation exhibit a breakdown of the global numerical resolution scheme at contact lengths in excess of 145 μm.

5.3. Effect of a slight misorientation of the crystal with respect to ideal orientation

It was indicated in Section 4.1.1 that the inclination of the observed slip traces could be attributed to misorientation of the crystal. It was also hypothesised that such a misorientation could also cause a bias in the activation of slip systems. To test this hypothesis, simulations using *Mesh 1* were launched. These simulations introduced a 10° misorientation in the crystal, introduced via a rotation about the *Z*-axis. Simulations with clockwise and anti-clockwise misorientation were tested. It was found that the simulation with the 10° misorientation in the clockwise direction yielded γ-maps closest to the experimentally observed slip traces. This dominant slip map is shown in Fig. 12.

The γ-maps in Fig. 12 shows that the activated slip systems are no longer symmetric, but are divided by a 'median' at an angle ≈ 11.5° to the axis of loading. It is also observed that the dominant slip regions strongly differ from those observed in Fig. 6(a). The regions in which system 12 was indicated as the dominant slip system are almost completely replaced by regions with system 7 as dominant slip, which is in agreement with the slip traces observed experimentally. This proves that any deviation from intended crystallographic axes can cause biased activation of slip systems. It is expected that the determination of the exact orientation of the crystal by means of Laue experiment can lead to even better agreement of the numerical predictions of slip activity and the experimental observations.

5.4. Stress fields and triaxiality

Fig. 13 presents stress maps in the specimen with the 10° misorientation (Orientation A with 10° rotation). It is observed that the stress distribution is asymmetric, and also that the highest stress is found not at the line of contact between the indent and the substrate, but at a distance of ≈ 260 μm from the indentation surface (Fig. 13(b)). This is typical of Hertzian contact. The analysis of such zones could be useful in the identification of the locations of damage initiation.

Another measure which can be used to characterise the complex nature of the stress state in a specimen is the *stress triaxiality*, which is defined as the ratio of the mean stress to the equivalent stress. The triaxiality was computed for the substrate used in the simulations. Fig. 14 shows the absolute values of the triaxiality at the core of the specimen. It was observed that the core of the specimen experiences substantial triaxiality in comparison with the free surface of the specimen, where the triaxiality is almost zero. This observation is in agreement with the reported observation in a previous publication (Sabnis et al., 2012), that the stress state at the core of an NBSX specimen is significantly different in comparison with the free surface, thereby necessitating a thorough 3D computational analysis of any NBSX specimen being considered.

6. Conclusions

The work presented here was aimed at a numerical analysis of cylindrical indentation tests using crystal plasticity, with the purpose of studying the applicability of crystal plasticity simulations to study sub-surface fields in NBSX materials. The simulations were compared with experimental observations of slip lines. The predicted plastic zone sizes were found to be in good agreement with plastic slip traces found on the surface of the specimen. The secondary orientation of the crystal was found to have a profound impact on the individual slip system activity and the plastic zone shape. Such activity further emphasises the necessity to study the effect of crystal plasticity on damage initiation and crack propagation in NBSX materials.

The simulations show that the strain fields and the lattice rotation fields predicted by CPFEM strongly differ on the lateral free surface and in the bulk. The transition zone in Orientation A (at a contact width of 140 μm) is found to be a boundary layer close to the surface having a thickness ≈ 320 μm. An analysis of the stress states at the core and the surface of the specimen also indicated that the peak stresses are found not at the indentation surface, but about 260 μm below the indentation surface. These observations demonstrate the importance of detailed 3D simulations of components for comparison with surface experimental observations.

Pile-up formations were reported in the indentation study discussed by Zambaldi et al. (2007) and also by Lee and Chen (2010) in the context of strain gradient plasticity applied to micro-indentation. In contrast to these reports, only sink-in was predicted by the numerical simulations presented here. This is related to the small hardening modulus of the considered material at room temperature.

In this work the computational and experimental analyses were limited to the determination of slip activity including dominant slip systems. Additional complementary experimental observations are required for more quantitative comparisons. They include roughness measurements at the indented surface to identify sink-in or pile-up situations, EBSD lattice rotation field measurements and strain field measurements on the lateral free surface.

References

Arakere, N.K., Swanson, G.R., 2001. Analysis of fretting stresses in single crystal Ni-base turbine blade attachment regions. ASME Journal of Tribology 123, 413–423.

Arakere, N.K., Swanson, G.R., 2002. Effect of crystal orientation on fatigue failure of single crystal Nickel base turbine blade superalloys. ASME Journal of Gas Turbines and Power 124, 161–176.

Arakere, N.K., Swanson, G.R., Duke, G., Ham-Battista, G., 2006. Subsurface stress fields in Face-Centred-Cubic single-crystal anisotropic contacts. Journal of Engineering for Gas Turbines and Power 128 (4), 879–888.

Asaro, R., 1983. Crystal plasticity. Journal of Applied Mechanics 50, 921–934.

Balint, D.S., Deshpande, V.S., Needleman, A., Van der Giessen, E., 2006. Discrete dislocation plasticity analysis of the wedge indentation of films. Journal of Mechanics and Physics of Solids 54, 2281–2303.

Besson, J., Foerch, R., 1997. Large scale object-oriented finite element code design. Computer Methods in Applied Mechanics and Engineering 142, 165–187.

Casals, O., Forest, S., 2009. Finite element crystal plasticity analysis of spherical indentation in bulk single crystals and coatings. Computational Materials Science 45, 774–782.

Chaboche, J.L., Cailletaud, G., 1996. Integration methods for complex constitutive equations. Computer Methods in Applied Mechanics and Engineering 133, 125–155.

Deluca, D., Annis, C., 1995. Fatigue in single crystal superalloys, Office of Naval Research, Tech. Rep. FR23800.

Deshpande, V.S., Needleman, A., Van der Giessen, E., 2004. Discrete dislocation plasticity analysis of static friction. Acta Materialia 52, 3135–3149.

Ebrahimi, F., Kalwani, K., 1999. Fracture anisotropy in silicon single crystal. Materials Science and Engineering 268A, 116–126.

Ebrahimi, F., Westbrooke, E.F., 2008. Effect of HIPping on deformation anisotropy in a single crystal Ni-based superalloy. Acta Materialia 56 (16), 4349–4357.

Ebrahimi, F., Forero, L.E., Siddiqui, S., Arakere, N.K., 2006. Effect of notch orientation on the evolution of plasticity in superalloy single crystals. Materials Science and Engineering: A 426, 214–220.

Eidel, B., 2011. Crystal plasticity finite-element analysis versus experimental results of pyramidal indentation into (001) fcc single crystal. Acta Materialia 59, 1761–1771.

Flouriot, S., Forest, S., Cailletaud, G., Köster, A., Rémy, L., Burgardt, B., Gros, V., Mosset, S., Delautre, J., 2003. Strain localization at the crack tip in single crystal CT specimens under monotonous loading: 3D Finite Element analyses and application to Nickel-base superalloys. International Journal of Fracture 124, 43–77.

Gumbsch, P., Riedle, J., Hartmaier, A., Fischmeister, H.F., 1998. Controlling factor for the ductile brittle-to-ductile transition in single crystals. Science 282, 1293–1295.

Jean, M., 1995. Frictional contact in collections of rigid or deformable bodies: numerical simulation of geomaterial motions. Studies in Applied Mechanics 42, 463–486.

Kysar, J.W., Briant, C.L., 2002. Crack tip deformation in ductile single crystals. Acta Materialia 50, 2367–2380.

Kysar, J.W., Gan, Y.X., Morse, T.L., Chen, X., Jones, M.E., 2007. High strain gradient plasticity associated with wedge indentation into face-centered cubic single crystals: geometrically necessary dislocation densities. Journal of Mechanics and Physics of Solids 55 (7).

Lee, W., Chen, Y., 2010. Simulation of micro-indentation hardness of fcc single crystals by mechanism-based strain gradient crystal plasticity. International Journal of Plasticity 26, 1527–1540.

Mandel, J., 1973. Equations constitutives et directeurs dans les mileux plastiques et viscoplastiques. International Journal of Solids and Structures 9, 725–740.

Méric, L., Poubanne, P., Cailletaud, G., 1991. Single crystal modeling for structural calculations. Part 1: Model presentation. Journal of Engineering Materials and Technology 113, 162–170.

Nalla, R.K., Campbell, J.P., Ritchie, R.O., 2002. Mixed-mode, high-cycle fatigue-crack growth thresholds in Ti–6Al–4V: role of small cracks. International Journal of Fatigue 24 (10), 1047.

Nicola, L., Bower, A.F., Kim, K.S., Needleman, A., Van der Giessen, E., 2007. Surface versus bulk nucleation of dislocations during contact. Journal of Mechanics and Physics of Solids 55, 1120–1144.

Nouailhas, D., Culie, J.P., Cailletaud, G., Méric, L., 1995. Finite-element analysis of the stress–strain behavior of single-crystal tubes. European Journal of Mechanics A: Solids 14 (1), 137–154.

Pierce, D., Asaro, R., Needleman, A., 1983. Material rate dependence and localized deformation in crystalline solids. Acta Metallurgica 31, 1951.

Ranjan, S., Arakere, N.K., 2008. A fracture mechanics based methodology for fatigue life prediction of single crystal Nickel based superalloys. ASME Journal for Gas Turbines and Power 130, 1–10.

Sabnis, P.A., Mazière, M., Forest, S., Arakere, N.K., Ebrahimi, F., 2012. Effect of secondary orientation on notch-tip plasticity in superalloy single crystals. International Journal of Plasticity 28, 102–123.

Shrivastava, S., Ebrahimi, F., 1997. Effect of crystallographic orientation on the fracture toughness of NIAL single crystals. MRS Proceedings 460, 392–398.

Tymiak, N.I., Krämer, D.E., Bahr, D.F., Wyrobek, T.J., Gerberich, W.W., 2001. Plastic strain and strain gradients at very small indentation depths. Acta Materialia 49, 1021–1034.

Westbrooke, E.F., 2005. Effect of crystallographic orientation on plastic deformation of single crystal nickel-base superalloys, Ph.D. dissertation, University of Florida Gainesville, Florida.

Wriggers, P., 2006. Computational Contact Mechanics. Springer, New York.

Xu, B., Yonezu, A., Yue, Z.F., Chen, X., 2009. Indentation creep surface morphology of nickel-based single crystal superalloys. Computational Materials Science 46, 275–285.

Xu, B.X., Wang, X.M., Zhao, B., Yue, Z.F., 2008. Study of crystallographic creep parameters of nickel-based single crystal superalloys by indentation method. Materials Science and Engineering A 478, 187–194.

Zambaldi, C., Roters, F., Raabe, D., Glatzel, U., 2007. Modeling and experiments on the indentation deformation and recrystallization of a single-crystal nickel-base superalloy. Materials Science and Engineering A 454–455, 433–440.

Zhu, T., Li, J., Van Vliet, K.J., Ogata, S., Yip, S., Suresh, S., 2004. Predictive modeling of nanoindentation-induced homogeneous dislocation nucleation in copper. Journal of Mechanics and Physics of Solids 52, 691–724.

Zienkiewicz, O.C., Pastor, M., Huang, M., 1995. Softening, localisation and adaptive remeshing. Capture of discontinuous solutions. Computational Mechanics 17, 98–106.